

RESEARCH ARTICLE

10.1002/2015SW001348

Key Points:

- We determine the 1 in 10, 1 in 50, and 1 in 100 events for energetic electrons in low Earth orbit
- The 1 in 10 year flux of $E > 30$ keV electrons lies in the range $1.8\text{--}6.6 \times 10^7 \text{ cm}^{-2} \text{ s}^{-1} \text{ sr}^{-1}$
- The $E > 30$ keV electrons have an upper limit in the range $5.1\text{--}8.8 \times 10^7 \text{ cm}^{-2} \text{ s}^{-1} \text{ sr}^{-1}$

Correspondence to:

N. P. Meredith,
nmer@bas.ac.uk

Citation:

Meredith, N. P., R. B. Horne, J. D. Isles, and J. C. Green (2016), Extreme energetic electron fluxes in low Earth orbit: Analysis of POES $E > 30$, $E > 100$, and $E > 300$ keV electrons, *Space Weather*, 14, 136–150, doi:10.1002/2015SW001348.

Received 30 NOV 2015

Accepted 22 JAN 2016

Accepted article online 28 JAN 2016

Published online 20 FEB 2016

©2016. The Authors.

This is an open access article under the terms of the Creative Commons Attribution License, which permits use, distribution and reproduction in any medium, provided the original work is properly cited.

Extreme energetic electron fluxes in low Earth orbit: Analysis of POES $E > 30$, $E > 100$, and $E > 300$ keV electrons

Nigel P. Meredith¹, Richard B. Horne¹, John D. Isles¹, and Janet C. Green²

¹British Antarctic Survey, Natural Environment Research Council, Cambridge, UK, ²Space Hazards Applications LLC, Golden, Colorado, USA

Abstract Energetic electrons are an important space weather hazard. Electrons with energies less than about 100 keV cause surface charging, while higher-energy electrons can penetrate materials and cause internal charging. In this study we conduct an extreme value analysis of the maximum 3-hourly flux of $E > 30$ keV, $E > 100$ keV, and $E > 300$ keV electrons in low Earth orbit as a function of L^* , for geomagnetic field lines that map to the outer radiation belt, using data from the National Oceanic and Atmospheric Administration Polar Operational Environmental Satellites (POES) from July 1998 to June 2014. The 1 in 10 year flux of $E > 30$ keV electrons shows a general increasing trend with distance ranging from $1.8 \times 10^7 \text{ cm}^{-2} \text{ s}^{-1} \text{ sr}^{-1}$ at $L^* = 3.0$ to $6.6 \times 10^7 \text{ cm}^{-2} \text{ s}^{-1} \text{ sr}^{-1}$ at $L^* = 8.0$. The 1 in 10 year flux of $E > 100$ keV electrons peaks at $L^* = 4.5\text{--}5.0$ at $1.9 \times 10^7 \text{ cm}^{-2} \text{ s}^{-1} \text{ sr}^{-1}$ decreasing to minima of 7.1×10^6 and $8.7 \times 10^6 \text{ cm}^{-2} \text{ s}^{-1} \text{ sr}^{-1}$ at $L^* = 3.0$ and 8.0 , respectively. In contrast to the $E > 30$ keV electrons, the 1 in 10 year flux of $E > 300$ keV electrons shows a general decreasing trend with distance, ranging from $2.4 \times 10^6 \text{ cm}^{-2} \text{ s}^{-1} \text{ sr}^{-1}$ at $L^* = 3.0$ to $1.2 \times 10^5 \text{ cm}^{-2} \text{ s}^{-1} \text{ sr}^{-1}$ at $L^* = 8.0$. Our analysis suggests that there is a limit to the $E > 30$ keV electrons with an upper bound in the range 5.1×10^7 to $8.8 \times 10^7 \text{ cm}^{-2} \text{ s}^{-1} \text{ sr}^{-1}$. However, the results suggest that there is no upper bound for the $E > 100$ keV and $E > 300$ keV electrons.

1. Introduction

Changes in the space environment, ultimately driven by the Sun, can significantly affect modern technological systems both on the ground and in space. As society becomes ever more heavily dependent on satellite technology, these changes, referred to as space weather, are becoming an increasingly important natural hazard risk. Severe space weather can damage critical infrastructure [Krausmann, 2011] and is even a potential risk to national security [Strategic National Risk Assessment, 2011]. Space weather was added to the UK National Risk Register of Civil Emergencies in 2012 [Cabinet Office, 2012] and is an ongoing topic of special collaboration between the UK and the U.S. [Viereck, 2012].

There are currently 1328 operational satellites in Earth orbit, being used for a variety of applications including communications, Earth observation, navigation, and military surveillance. These satellites operate in various orbits around the Earth of which 676 are in low Earth orbit (LEO), 519 in geosynchronous orbit, 91 in medium Earth orbit, and 42 in elliptical orbit (www.satellites.findthedata.com). In 2014 the total revenue from the satellite industry was U.S. \$203 billion [Satellite Industry Association, 2015], showing the importance of the industry on the economy. One recent report estimates that the loss of revenue from satellite services alone, for an event 3 times the size of the Carrington event of 1859, could be as high as U.S. \$30 billion [Odenwald and Green, 2007]. However, there is a large uncertainty associated with this estimate, and the likely effect of a severe space weather storm on the satellite fleet remains difficult to quantify.

Space weather can affect satellites in a number of ways. Galactic cosmic rays and solar particle events cause single-event upsets. The latter also causes displacement damage which leads to degradation of solar array power. Energetic electrons affect satellites in two principle ways, depending on energy. Electrons with energies in the range from \sim keV to \sim 100 keV, which are injected into the inner magnetosphere during storms and substorms [Cayton et al., 1989], affect the current balance to the satellite surface. This may result in a high level of surface charging [e.g., Koons and Gorney, 1992; Koons and Fennell, 2006], especially when the satellite is in eclipse. Different materials on the surface of a satellite respond differently to the various charging sources resulting in differential surface charging. This may lead to the buildup of charge between various satellite surfaces, the subsequent discharge of which can damage surface materials and underlying

components. Higher-energy electrons, which tend to build up during geoeffective storms and geoeffective high-speed solar wind streams, can penetrate surface materials and embed themselves within insulators. Such charging, known as internal charging, can lead to the buildup of significant amounts of charge, the subsequent discharge of which can damage components [e.g., *Koons and Gorney, 1992; Wrenn, 1995; Gubby and Evans, 2002*].

Low Earth orbit is an orbit close to the Earth, typically at altitudes between 300 km and 800 km. It is a particularly important orbit for Earth observation and military surveillance, since satellites located in this orbit are best placed for obtaining high-resolution images of the Earth. Satellites in LEO with inclinations greater than about 40° are exposed to electrons injected into the inner magnetosphere during storms and substorms and, at higher energies, to electrons in the radiation belts. Such exposure can damage or even prove fatal for a satellite. For example, on 24 October 2003 the joint Japanese/U.S. Midori-2 environmental research satellite suffered a catastrophic failure [*Webb and Allen, 2004*]. The cause of the failure has since been extensively studied and attributed to sustained arcs on the solar array paddle or paddle harness caused by substorm-injected electrons in the auroral zone [*Maejima et al., 2004*].

Modern LEO satellites are typically designed to operate for 10 to 15 years. Satellite operators and engineers, therefore, require realistic estimates of the highest flux levels that may be encountered on these and longer timescales to help assess how hostile the spacecraft environment could become in a worst-case scenario. These estimates can then be used to help assess the impact of extreme events on the satellite fleet and to improve the resilience of future satellites by better design of satellite components. Satellite insurers also require this information to help them evaluate realistic disaster scenarios.

In this study we used 16 years of data from the National Oceanic and Atmospheric Administration (NOAA) Polar Operational Environmental Satellites (POES) to determine the 1 in 10, 1 in 50, and 1 in 100 year space weather events for energetic electrons at LEO as a function of the magnetic coordinate L^* , for geomagnetic field lines that map to the outer radiation belt. Specifically, we used the 2 s resolution $E > 30$ keV, $E > 100$ keV, and $E > 300$ keV electron data from NOAA 15 to NOAA 19 from 1 July 1998 to 30 June 2014. We sorted it according to satellite location, corrected for ring current protons, and excluded solar proton events and periods of poor quality data. We calculated the maximum flux in each 3 h window as a function of energy and L^* . We then determined the number of times the maximum fluxes rose above given thresholds and computed probability distribution functions, as a function of energy and L^* . We then conducted an extreme value analysis to determine the 1 in 10, 1 in 50, and 1 in 100 year space weather events at LEO as a function of energy and L^* .

2. Instrumentation and Data Analysis

The particle data used in this study were collected by the Medium Energy Proton and Electron Detector (MEPED) on board the NOAA POES satellites. These satellites orbit the Earth approximately 14 times each day in Sun-synchronous, low-altitude, polar orbits. Here we use data from NOAA 15 to NOAA 19 (Table 1).

The MEPED instrument includes two electron solid-state detector telescopes that measure the flux of electrons in three energy bands in the range 30–2500 keV and two proton solid-state detector telescopes that measure the flux of protons in the energy range 30–6900 keV [*Evans and Greer, 2004*]. For each detector telescope pair, one, called the 0° telescope, T0, is aligned such that the center of its field of view is rotated 9° from the direction outward along the local zenith. The other, called the 90° telescope, T90, is mounted perpendicular to T0 such that the center axis of its field of view is rotated 9° from the direction antiparallel to the direction of the spacecraft velocity. Since the field of view of each telescope is 30° , at 55° – 68° invariant latitude, on field lines that map to the outer radiation belt, the T90 detector measures a mix of particles which may be in the bounce or drift loss cone or stably trapped [*Rodger et al., 2010b*] while the T0 telescope measures the precipitating flux inside the bounce loss cone [*Rodger et al., 2010a*]. The T90 fluxes are larger than the T0 fluxes, especially at lower L^* , and since we are interested in the largest fluxes that may be encountered, we select the T90 measurements for this study. Data from each detector are accumulated for 1 s, and since the electronics are shared between the two detectors, data from each detector are collected at a 2 s time resolution.

The POES electron data were initially downloaded at a 2 s time resolution. Data flagged as of poor quality and data recorded when MEPED in flight calibrations were in progress were excluded from the subsequent analysis. Spikes are occasionally observed in the 2 s data that are orders of magnitude larger than neighboring values. These were removed by replacing the spike value, defined as being 10 or more times larger than its two

Table 1. NOAA POES Satellites Used in Study

Satellite	Altitude (km)	Inclination (deg)	Period (min)	Local Time of Ascending Node	Data Window
NOAA 15	807	98.5	101.1	16:50	1/7/1998 to 30/6/2014
NOAA 16	849	99.0	102.1	17:31	10/1/2001 to 9/6/2014
NOAA 17	810	98.7	101.2	21:34	12/7/2002 to 10/4/2013
NOAA 18	854	98.7	102.1	13:41	7/6/2005 to 30/6/2014
NOAA 19	870	98.7	102.1	14:10	2/6/2009 to 30/6/2014

nearest neighbors, with the average value from the two neighboring values. The measured electron fluxes can become contaminated during solar proton events. We excluded these intervals by adopting the NOAA Space Weather Prediction Center’s definition of a solar proton event and excluded data whenever the flux of $E > 10$ MeV protons determined from the Geostationary Operational Environmental Satellite (GOES) Energetic Particle Sensor measurements was greater than $10 \text{ cm}^{-2} \text{ s}^{-1} \text{ sr}^{-1}$. The flux measurements from the electron detector telescopes were then corrected for ring current protons as described by *Lam et al.* [2010]. Since the electron flux falls rapidly with increasing energy, we ensured that the $E > 30$ keV flux was greater than the $E > 100$ keV flux which was in turn greater than the $E > 300$ keV flux to exclude bit errors.

Electrons with energies of the order of tens of keV are injected on the nightside and drift around dawn to the dayside. Figure 1 (left) shows a global statistical map of the flux of $E > 30$ keV electrons observed by the T90 detector during active conditions ($AE > 300$ nT) as a function of L and magnetic local time (MLT). The plots extend linearly out to $L = 9$ with noon at the top and dawn to the right. The average fluxes tend to be highest primarily on the dawnside from 22:00 to 13:00 MLT with a minimum near dusk. Figure 1 (middle and right) shows the average fluxes of $E > 100$ keV and $E > 300$ keV electrons during active conditions in the same format. The fluxes of $E > 100$ keV electrons maximize on the dawnside, but large fluxes can also be seen on the duskside. At higher energies the flux of $E > 300$ keV electrons does not vary significantly with local time. We choose a 3 h window for our analysis to get good coverage on the field lines that map to the regions of enhanced fluxes of energetic electrons in the outer radiation belt. For example, during any given 3 h window any given POES satellite will pass four times through field lines that map to the region of enhanced $E > 30$ keV electrons and eight times through field lines that map to the region of enhanced $E > 100$ keV and $E > 300$ keV electrons.

Since surface charging can occur on fast timescales, of the order of seconds for absolute charging and minutes for differential charging [Rodgers and Ryden, 2001], we select the 2 s resolution data for the analysis. To get a representative measure of the largest flux in any given 3 h period, we determined the maximum observed flux as a function of energy and L^* using the electron data from all available satellites in that period. Here L^* is related to the third adiabatic invariant, Φ , and is given by

$$L^* = \frac{-2\pi k_0}{\Phi R_E} \tag{1}$$

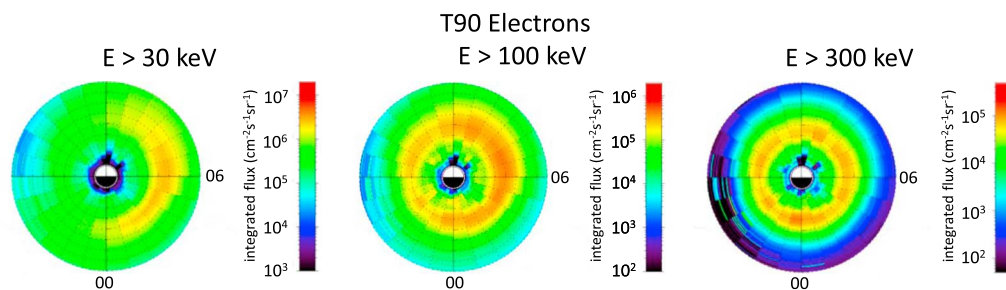


Figure 1. Plot of the average integrated flux of (left) $E > 30$ keV, (middle) $E > 100$ keV, and (right) $E > 300$ keV electrons as a function of L and MLT during active conditions. The plots extend linearly out to $L = 9$ with noon at the top and dawn to the right.

where k_0 is the Earth's magnetic dipole moment. Physically, L^* is the radial distance in Earth radii to the equatorial points of the symmetric shell on which the particles would be found if all the nondipolar components of the trapping magnetic field were adiabatically removed [Roederer, 1970]. The resulting maximum electron flux in each 3 h period was then binned as a function of energy, L^* , and UT time at a resolution of $0.1 L^*$. To maximize the use of the available data, we then smoothed the data as a function of L^* using a running four-point average. We here and henceforth refer to the maximum fluxes so determined in the $30 < E < 2500$ keV, the $100 < E < 2500$ keV, and the $300 < E < 2500$ keV electron channels, as the $E > 30$ keV, $E > 100$ keV, and $E > 300$ keV electron fluxes. This resulted in $44,092 \pm 2$ good quality data points at each energy and L^* , corresponding to 15.1 years of operational data. L^* was computed using the UNILIB software library (<http://www.mag-unilib.eu/>), using the International Geomagnetic Reference Field at the start of the appropriate year and the Olson-Pfitzer quiet time model [Olson and Pfitzer, 1977]. The solar wind parameters and the geomagnetic indices were stored at a 1 h resolution.

3. Statistics

As a visual aid we first plotted the electron fluxes as a function of time for each energy and L^* to make sure that there were no outliers or unforeseen peculiarities in the data. An example overview plot for April 2010, containing the time when Galaxy 15 stopped responding to ground commands [e.g., Loto'aniu et al., 2015], is shown in Figure 2. To put the data in context, in addition to the POES electron fluxes, the plots also show relevant geophysical indices and solar wind parameters and the GOES $E > 2$ MeV electron flux. Figure 2 shows (a) the GOES $E > 2$ MeV electron flux; (b–g) the POES $E > 30$ keV electron flux for $L^* = 8.0, 7.0, 6.0, 5.0, 4.0,$ and 3.0 , respectively; (h) the solar wind speed (red trace) and interplanetary magnetic field (IMF) B_z (black trace); (i) the Dst index (color coded) and solar wind pressure (red trace); and (j) the Kp (color coded) and AE (black trace) indices. The vertical dashed line in each panel represents the time of the Galaxy 15 anomaly. In the panels showing the POES electron flux the symbols represent the T90 electron fluxes used in this analysis and the purple traces represent the T0 electron fluxes. The dotted lines in the panels showing the POES electron fluxes represent the 0.1% exceedance levels of the T90 fluxes for the plotted L^* . The T90 data symbols are coded red above and black below the 0.1% exceedance level in each panel.

During this period there were two moderate storms as evidenced by the Dst index, with minimum $Dst < -50$ nT (Figure 2i), together with periods of substorm activity as monitored by the AE index in the absence of significant storm signatures (Figure 2k). Substorm injections are associated with sudden increases in the flux of electrons in both the T90 and T0 channels. They are most prevalent in the outer region, typically at or beyond $L^* = 6.0$. Closer in, substorm injections are associated with stronger periods of magnetic activity. The Galaxy 15 anomaly occurred on 5 April at 09:48 UT at the start of the main phase of a moderate geomagnetic storm, with minimum Dst of -81 nT on 6 April (Figure 2i). At the time of the anomaly the Kp index was 8^- and the AE index was 1419 nT indicating very strong geomagnetic and substorm activity, respectively (Figure 2j). There were enhanced fluxes of $E > 30$ keV electrons from $L^* = 8.0$ to $L^* = 3.0$ (Figures 2b–2g). Fluxes of $E > 100$ and $E > 300$ keV electrons were also enhanced (not shown), but the fluxes of $E > 2$ MeV electrons (Figure 2a) were not enhanced, being a factor of about 2 orders of magnitude less than the fluxes of $E > 2$ MeV electrons subsequently observed from 7 to 11 April during the storm recovery phase.

Monthly and yearly overview plots were plotted in this format for the $E > 30$, $E > 100$, and $E > 300$ keV electrons and inspected for outliers. Careful inspection of the data as a function of time for each energy and L^* revealed the very occasional outlier that was an order of magnitude or more larger than its nearest neighbors. Substorm injections can lead to large flux increases, but they tend to be associated with large flux increases in both the T90 and T0 detectors. However, the majority of the outliers were not associated with concomitant increases in the T0 fluxes and were an order of magnitude more than the T0 fluxes. The outliers were automatically removed by replacing them with the average value from their neighbors whenever the T90 flux was more than 10 times the T90 flux immediately prior and following and 20 times greater than the T0 flux. For the 11 L^* values in the range from 3.0 to 8.0 in steps of 0.5 we identified and replaced a total of 33, 113, and 116 outliers for the $E > 30$, $E > 100$, and $E > 300$ keV electrons, respectively. A number of outliers remained in the high-energy channel at high L^* ($L^* \geq 6.5$), and these were removed irrespective of the value of the T0 fluxes.

The largest fluxes of the $E > 30$, $E > 100$, and $E > 300$ keV electron channels at $L^* = 4.5$ and $L^* = 6.0$ are tabulated in Tables 2 and 3, respectively. The largest flux of $E > 30$ keV electrons observed at $L^* = 6.0$, on field lines that map out close to geosynchronous orbit, was $6.2 \times 10^7 \text{ cm}^{-2} \text{ s}^{-1} \text{ sr}^{-1}$ on 24 April 2012. We note

NOAA 15, 16, 17, 18 & 19 and GOES 11 Energetic Electrons

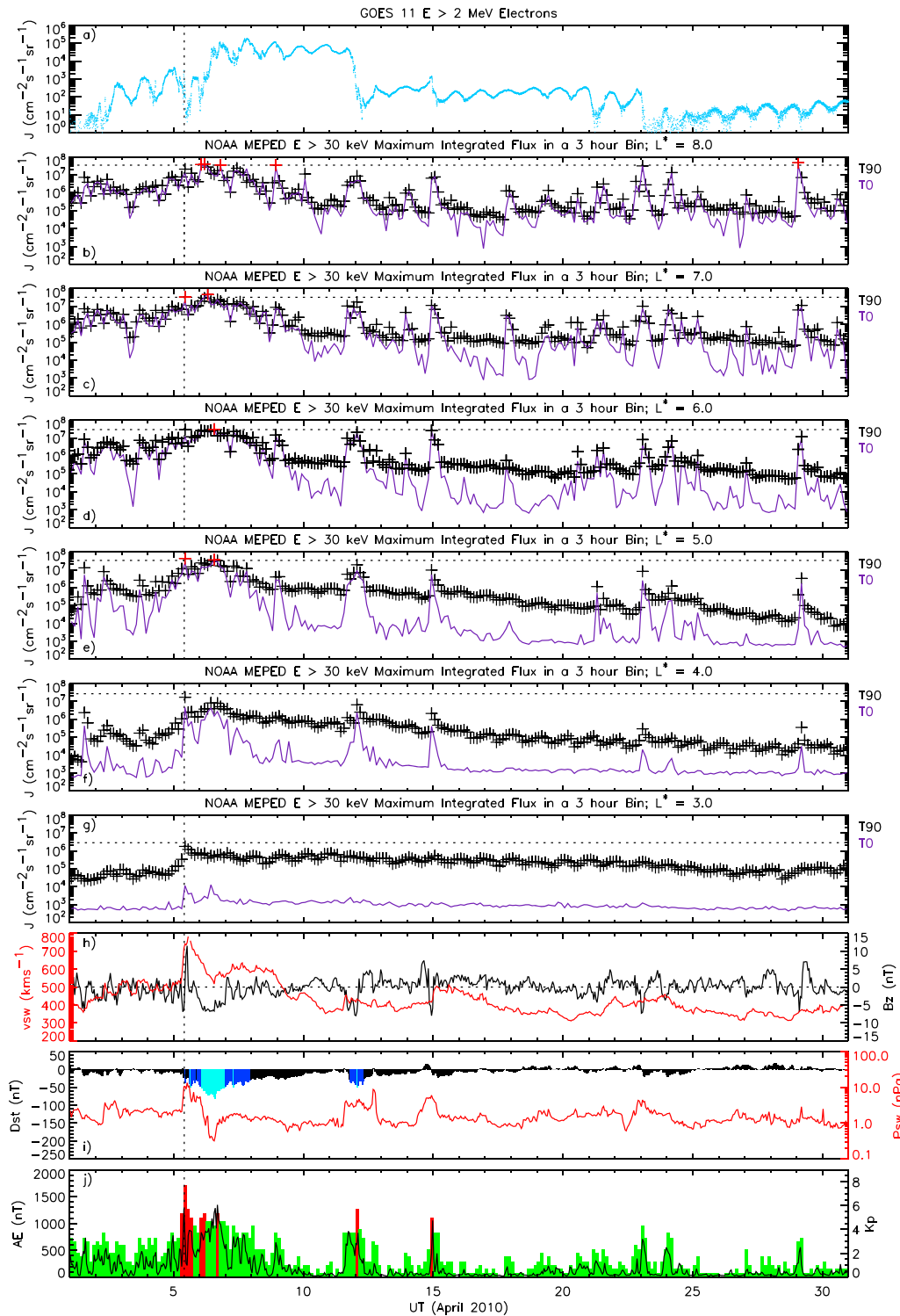


Figure 2. Summary plot of the POES $E > 30$ keV electron fluxes for April 2010. (a) The GOES 11 $E > 2$ MeV electron flux; (b–g) the POES $E > 30$ keV electron flux at $L^* = 8.0, 7.0, 6.0, 5.0, 4.0,$ and $3.0,$ respectively; (h) the solar wind speed (red trace) and IMF B_z (black trace); (i) the Dst index (color coded) and solar wind pressure (red trace); and (j) the K_p (color coded) and AE (black trace) indices. The vertical dashed line in each of the panels represents the time of the Galaxy 15 anomaly. In the POES electron flux panels the symbols represent the T90 electron fluxes, the purple traces represent the T0 electron fluxes, and the dotted lines represent the 0.1% exceedance levels. The T90 data symbols are coded red above and black below the 0.1% exceedance level in each panel.

Table 2. Largest $E > 30$, $E > 100$, and $E > 300$ keV Electron Fluxes Observed at $L^* = 4.5$

$E > 30$ keV Flux ($\text{cm}^{-2} \text{s}^{-1} \text{sr}^{-1}$)	Date	$E > 100$ keV Flux ($\text{cm}^{-2} \text{s}^{-1} \text{sr}^{-1}$)	Date	$E > 300$ keV Flux ($\text{cm}^{-2} \text{s}^{-1} \text{sr}^{-1}$)	Date
5.0×10^7	20 Nov 2003 15–18	2.6×10^7	21 Jul 2005 00–03	2.6×10^6	21 Jul 2005 00–03
4.8×10^7	17 Mar 2003 15–18	1.9×10^7	16 Jun 2003 21–24	2.4×10^6	5 Apr 2010 09–12
4.8×10^7	16 Jun 2003 21–24	1.7×10^7	5 Apr 2010 09–12	1.2×10^6	18 Aug 2003 09–12
4.6×10^7	30 Apr 2005 12–15	1.5×10^7	17 Sep 2003 12–15	1.2×10^6	6 Apr 2010 09–12
4.6×10^7	22 Oct 2001 12–15	1.5×10^7	20 Mar 2001 12–15	1.1×10^6	6 Apr 2010 18–21
4.5×10^7	21 Jul 2005 00–03	1.5×10^7	8 May 2005 12–15	1.0×10^6	14 Apr 2006 09–12
4.4×10^7	18 Feb 1999 03–06	1.5×10^7	18 Aug 2003 09–12	1.0×10^6	7 Apr 2010 00–03
4.3×10^7	14 Apr 2006 09–12	1.4×10^7	12 Jun 2005 18–21	1.0×10^6	7 Apr 2010 03–06
4.3×10^7	1 Apr 2003 00–03	1.4×10^7	8 May 2005 12–15	9.8×10^5	6 Apr 2010 21–24
4.2×10^7	18 Apr 2002 06–09	1.3×10^7	14 Apr 2006 09–12	9.8×10^5	25 Jul 2004 09–12

that at the magnetic equator the T90 electrons have a small pitch angle, of the order of 3° . Electrons with larger equatorial pitch angles are therefore likely to have larger fluxes due to anisotropies in the pitch angle distribution, but these cannot be measured at POES altitudes. The largest flux of $E > 30$ keV electrons at $L^* = 4.5$, on field lines that typically map out to the vicinity of the perigees of the European Galileo satellites, was $5.0 \times 10^7 \text{ cm}^{-2} \text{ s}^{-1} \text{ sr}^{-1}$ on 20 November 2003. At higher energies, the largest fluxes of $E > 100$ keV electrons at $L^* = 6.0$ and 4.5 were factors of 3 and 2 lower at $1.9 \times 10^7 \text{ cm}^{-2} \text{ s}^{-1} \text{ sr}^{-1}$, recorded on 16 April 2003, and $2.6 \times 10^7 \text{ cm}^{-2} \text{ s}^{-1} \text{ sr}^{-1}$, recorded on 21 July 2005. In the highest-energy channel the largest fluxes of $E > 300$ keV electrons at $L^* = 6.0$ and 4.5 were factors of 25 and 10 lower than the maximum $E > 100$ keV fluxes at $7.7 \times 10^5 \text{ cm}^{-2} \text{ s}^{-1} \text{ sr}^{-1}$, recorded on 6 April 2010, and $2.6 \times 10^6 \text{ cm}^{-2} \text{ s}^{-1} \text{ sr}^{-1}$, recorded on 21 July 2005, respectively.

We then determined the number of times the flux exceeded certain thresholds as a function of L^* and energy. The results are tabulated in Table 4. Large fluxes of $E > 30$ keV electrons were most prevalent in the region $4.5 < L^* < 8.0$. The number of times the flux exceeded $5 \times 10^6 \text{ cm}^{-2} \text{ s}^{-1} \text{ sr}^{-1}$ reached a peak value of 5296 at $L^* = 6.0$. At higher energies the largest fluxes of $E > 100$ keV electrons were most prevalent in the region $4.5 \leq L^* \leq 6.0$. Here the maximum in the number of times the flux exceeded $2 \times 10^6 \text{ cm}^{-2} \text{ s}^{-1} \text{ sr}^{-1}$ occurred closer in at $L^* = 5.0$. In the highest-energy channel, the largest fluxes of $E > 300$ keV electrons were most prevalent further in, typically in the region $3.0 \leq L^* \leq 4.5$. Here the number of times the flux exceeded $5 \times 10^5 \text{ cm}^{-2} \text{ s}^{-1} \text{ sr}^{-1}$ reached a peak value of 636 at $L^* = 4.0$.

The distribution of the flux of $E > 30$ keV electrons is shown as a function of L^* in Figure 3a. To highlight the extremes of the distribution, we plotted the exceedance probabilities, $P(J > j)$, representing the probability that an individual sample J exceeds a threshold j . The observed fluxes cover over 4 orders of magnitude

Table 3. Largest $E > 30$, $E > 100$, and $E > 300$ keV Electron Fluxes Observed at $L^* = 6.0$

$E > 30$ keV Flux ($\text{cm}^{-2} \text{s}^{-1} \text{sr}^{-1}$)	Date	$E > 100$ keV Flux ($\text{cm}^{-2} \text{s}^{-1} \text{sr}^{-1}$)	Date	$E > 300$ keV Flux ($\text{cm}^{-2} \text{s}^{-1} \text{sr}^{-1}$)	Date
6.2×10^7	24 Apr 2012 06–09	1.9×10^7	16 Apr 2003 09–12	7.7×10^5	6 Apr 2010 09–12
5.3×10^7	25 Jul 2004 09–12	1.3×10^7	25 Jul 2004 09–12	4.3×10^5	5 Apr 2010 09–12
5.1×10^7	20 Nov 2003 15–18	1.2×10^7	10 Dec 2003 15–18	4.2×10^5	23 Jul 2004 06–09
4.9×10^7	18 Jun 2012 03–06	1.1×10^7	8 May 2003 15–18	3.7×10^5	23 Jul 2004 09–12
4.2×10^7	31 Mar 2001 15–18	1.0×10^7	27 Mar 2008 03–06	3.2×10^5	14 Apr 2006 06–09
4.2×10^7	12 Jul 2003 03–06	9.8×10^6	5 Apr 2010 09–12	3.0×10^5	17 Jun 2003 09–12
4.1×10^7	16 Apr 2003 09–12	9.7×10^6	12 Jun 2005 18–21	3.0×10^5	10 May 2003 00–03
4.0×10^7	10 May 2003 09–12	9.7×10^6	17 Nov 2003 12–13	2.7×10^5	16 Apr 2003 09–12
3.9×10^7	16 Mar 2003 18–21	9.7×10^6	25 Jul 2004 09–12	2.6×10^5	21 Dec 2006 06–09
3.8×10^7	24 Oct 2003 15–18	9.4×10^6	23 Jul 2004 06–09	2.5×10^5	6 Apr 2010 15–18

Table 4. Number of Times Flux Exceeds Certain Thresholds

L^*	$E > 30$ keV				$E > 100$ keV			$E > 300$ keV		
	5×10^6 ($\text{cm}^2 \text{ s sr}^{-1}$)	10^7 ($\text{cm}^2 \text{ s sr}^{-1}$)	2×10^7 ($\text{cm}^2 \text{ s sr}^{-1}$)	2×10^6 ($\text{cm}^2 \text{ s sr}^{-1}$)	5×10^6 ($\text{cm}^2 \text{ s sr}^{-1}$)	10^7 ($\text{cm}^2 \text{ s sr}^{-1}$)	5×10^5 ($\text{cm}^2 \text{ s sr}^{-1}$)	10^6 ($\text{cm}^2 \text{ s sr}^{-1}$)	2×10^6 ($\text{cm}^2 \text{ s sr}^{-1}$)	
3.0	25	6	3	196	10	1	378	88	23	
3.5	141	59	17	196	18	1	584	100	4	
4.0	657	297	86	327	57	11	636	29	0	
4.5	1832	907	252	704	151	18	284	8	2	
5.0	3509	1713	352	982	177	18	48	5	1	
5.5	4922	2147	344	896	138	17	10	3	0	
6.0	5296	1894	268	619	78	5	1	0	0	
6.5	4645	1372	188	333	36	4	0	0	0	
7.0	3482	996	155	177	20	2	0	0	0	
7.5	2453	664	136	108	15	2	0	0	0	
8.0	1698	505	138	71	14	0	0	0	0	

ranging from 2×10^3 to $7 \times 10^7 \text{ cm}^{-2} \text{ s}^{-1} \text{ sr}^{-1}$. The largest observed $E > 30$ keV flux ranges from $3 \times 10^7 \text{ cm}^{-2} \text{ s}^{-1} \text{ sr}^{-1}$ at $L^* = 3.0$ to $7 \times 10^7 \text{ cm}^{-2} \text{ s}^{-1} \text{ sr}^{-1}$ at $L^* = 8.0$. The flux levels that are exceeded 5%, 1%, and 0.1% of the time are shown in Figure 3d. The 5%, 1%, and 0.1% flux exceedance levels maximize at $L^* = 5.5, 5.0,$ and $5.0,$ respectively.

The distribution of the flux of $E > 100$ keV electrons is shown in Figure 3b. The observed fluxes cover over 4 orders of magnitude ranging from 10^3 to $3 \times 10^7 \text{ cm}^{-2} \text{ s}^{-1} \text{ sr}^{-1}$. The largest observed $E > 100$ keV flux ranges from $10^7 \text{ cm}^{-2} \text{ s}^{-1} \text{ sr}^{-1}$ at $L^* = 8.0$ to $3 \times 10^7 \text{ cm}^{-2} \text{ s}^{-1} \text{ sr}^{-1}$ at $L^* = 5.0$. The flux levels that are exceeded 5%,

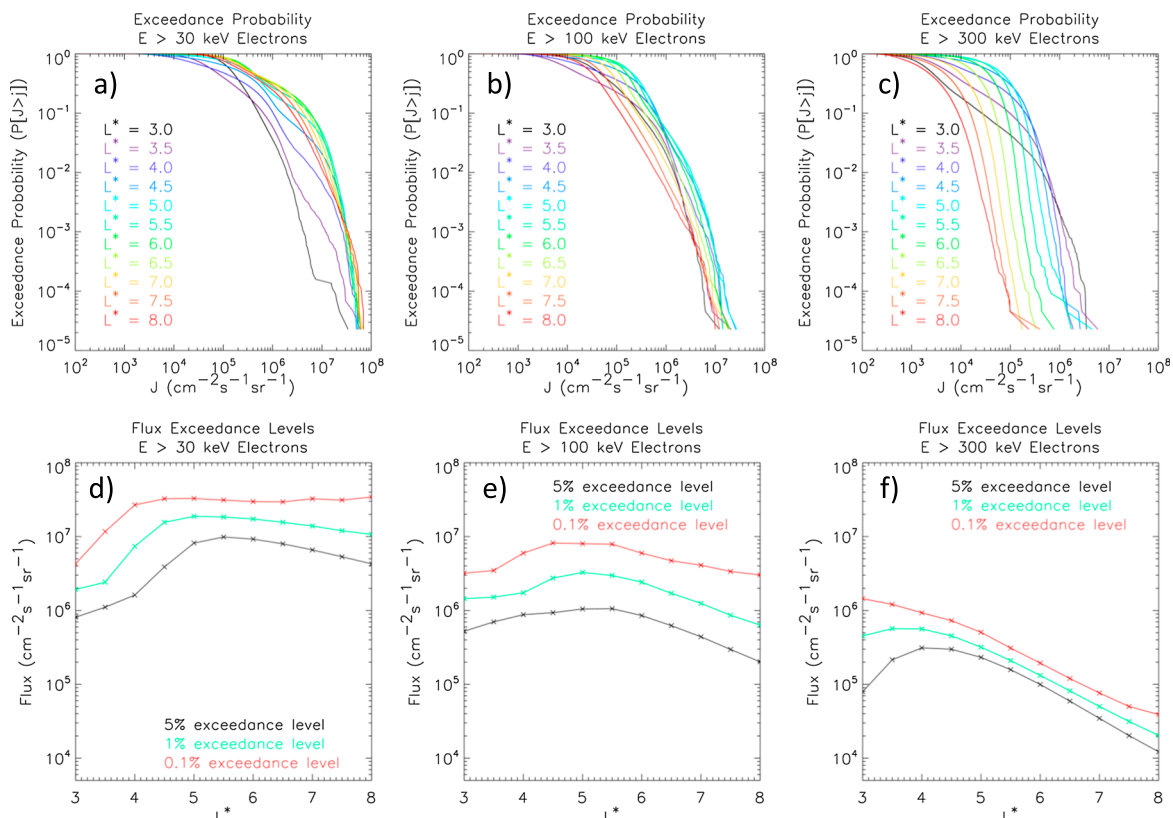


Figure 3. Plots of the exceedance probabilities for (a) $E > 30$ keV, (b) $E > 100$ keV, and (c) $E > 300$ keV electron fluxes for different L^* values and the 5% (black), 1% (green), and 0.1% (red) flux exceedance levels as a function of L^* for (d) $E > 30$ keV, (e) $E > 100$ keV, and (f) $E > 300$ keV electron fluxes.

1%, and 0.1% of the time are shown in Figure 3e. The 5%, 1%, and 0.1% flux exceedance levels maximize at $L^* = 5.5, 5.0,$ and $4.5,$ respectively.

The distribution of the flux of $E > 300$ keV electrons is shown in Figure 3c. The observed fluxes cover over 4 orders of magnitude ranging from 10^2 to $6 \times 10^6 \text{ cm}^{-2} \text{ s}^{-1} \text{ sr}^{-1}$. The largest observed $E > 300$ keV flux ranges from $2 \times 10^5 \text{ cm}^{-2} \text{ s}^{-1} \text{ sr}^{-1}$ at $L^* = 6.0$ to $7 \times 10^6 \text{ cm}^{-2} \text{ s}^{-1} \text{ sr}^{-1}$ at $L^* = 3.5$. The flux levels that are exceeded 5%, 1%, and 0.1% of the time are shown in Figure 3f. The 5%, 1%, and 0.1% flux exceedance levels maximize at $L^* = 4.0, 3.5,$ and $3.0,$ respectively.

4. Extreme Value Analysis

In order to calculate the 1 in N year event, we conducted an extreme value analysis of the $E > 30$ keV, $E > 100$ keV, and $E > 300$ keV electron data as a function of L^* . There are two main methods of calculating extreme values: one uses block maxima and the other uses exceedances over a high threshold. The exceedances over a threshold approach make the best use of the available data and have been successfully applied in many fields to estimate, for example, extremes of surface temperature [Nogaj et al., 2006], rainfall [Li et al., 2005], wind speed [Della-Marta et al., 2009], storm surge [Tebaldi et al., 2012], and geomagnetic activity [Tsubouchi and Omura, 2007; Thomson et al., 2011]. It has also been used to estimate extreme fluxes of relativistic electrons at geosynchronous orbit [Koons, 2001; Meredith et al., 2015], and we chose the same approach here. In this case the appropriate distribution function is the generalized Pareto distribution (GPD), first introduced by Picklands [1975].

Following Coles [2001], the GPD, $G(y)$, may be written in the form

$$G(y) = 1 - \left(1 + \frac{\xi y}{\sigma}\right)^{-\frac{1}{\xi}} \tag{2}$$

where $y = (x - u)$ are the exceedances and x are the data values above the chosen threshold, u . The GPD is characterized by two parameters, a shape parameter, ξ , and a scale parameter, σ . The former controls the behavior of tail of the distribution, and the latter determines the statistical dispersion of the distribution. If $\xi < 0$, the distribution of exceedances has an upper bound, whereas if $\xi > 0$, the distribution has no upper limit. The GPD is itself a distribution function, with $1 - G(y)$ representing the probability that a random variable X exceeds some value x given that it already exceeds a threshold u , $P(X > x | X > u)$.

The quality of a fitted GPD model may be assessed by comparing the empirical and modeled probabilities and quantiles [Coles, 2001]. For probabilities the modeled probability, $G(y)$, is plotted against the empirical probability. Assuming threshold exceedances $y(1) \leq \dots \leq y(k)$ and an estimated model G , the probability plot consists of the pairs

$$\left(\frac{i}{k+1}, G(y_{(i)})\right); i = 1, \dots, k \tag{3}$$

For the quantiles, the empirical exceedances are plotted against the modeled exceedances, y . The quantile plot then consists of the pairs

$$\left(G^{-1}\left(\frac{i}{k+1}\right), y_{(i)} + u\right); i = 1, \dots, k \tag{4}$$

where

$$G^{-1}(y) = u + \frac{\sigma}{\xi} ((1 - y)^{-\xi} - 1) \tag{5}$$

If the generalized Pareto model is a good method for modeling the exceedances, y , then both the probability and quantile plots should be approximately linear.

We are primarily interested in the largest flux that is likely to be observed over a given period of time. Following Coles [2001], the level, x_N , which is exceeded on average once every N years is given by

$$x_N = u + \frac{\sigma}{\xi} ((N n_d \zeta_u)^\xi - 1), \tag{6}$$

where ζ_u is the probability of an individual observation exceeding the threshold and $n_d = 2922$ is the average number of data points in any given year. A plot of x_N against N is known as a return level plot.

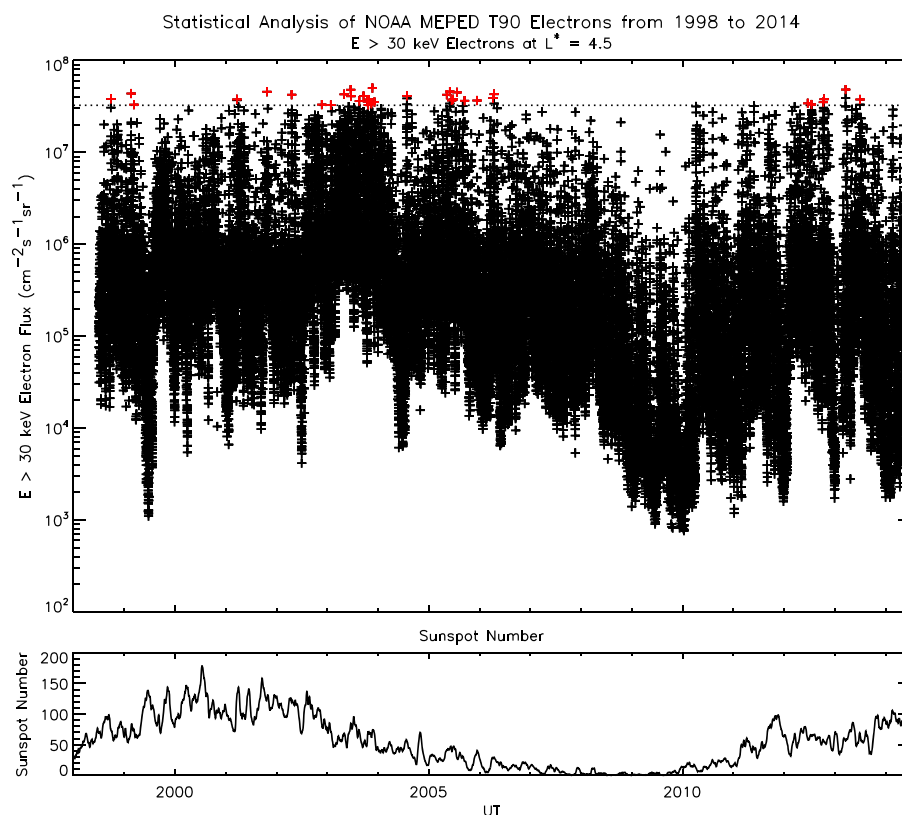


Figure 4. Plot of the $E > 30$ keV electron fluxes as a function of UT at $L^* = 4.5$. (top) The 0.1% exceedance level, chosen as the threshold for the extreme value analysis, is shown as a dotted line and the cluster maxima are coded red. (bottom) Trace of the sunspot number as a function of UT.

Observations show that there is a tendency for the data to cluster, in that a 3 h period with a high maximum flux can be exceeded by another. This breaks the assumption used in the statistical analysis that the individual exceedances should be independent. The most widely used method for dealing with this issue is known as declustering. We binned the groups of the data when the threshold is exceeded into clusters, including periods when the threshold is only exceeded once. We then identified the cluster maxima and assumed that the cluster maxima are independent with conditional exceedances given by the GPD. We used an empirical rule to determine clusters of exceedances, depending on the general temporal behavior of the flux at a given energy and L^* . In the two lowest-energy channels the temporal behavior of the electrons is characterized by frequent injections down to $L^* = 4.0$. For these energies and for $L^* \geq 4.0$ we considered a cluster to be active until three consecutive 3-hourly maxima fall below our chosen threshold. At lower L^* the temporal behavior of the two lowest-energy channels is characterized by relatively infrequent injections followed by slow decays lasting many days. During these decays the T90 population can become orders of magnitude larger than the T0 population and a small diurnal variation may become evident in the T90 flux due to sampling effects. This diurnal variation may potentially impact the cluster selection if a cluster is considered to be active for less than eight consecutive 3-hourly maxima. Inside $L^* = 4.0$ we therefore consider a cluster to be active until eight consecutive 3-hourly maxima fall below our chosen threshold. In the highest-energy channel the fluxes typically increase gradually over a period of days and then gradually decay over tens of days. During the decay period sampling effects again become apparent so we considered a cluster to be active until eight consecutive 3-hourly maxima fell below our chosen threshold. We then fitted the GPD to the cluster maxima. In this case ζ_u is given by n_c/n_{tot} where n_c is the number of clusters and n_{tot} the total number of data points.

We fitted the GPD to the cluster maxima as a function of energy and L^* by maximum likelihood estimation using the routine `gpd.fit` provided in the library `ismev` [Heffernan *et al.*, 2014] of the R statistical language

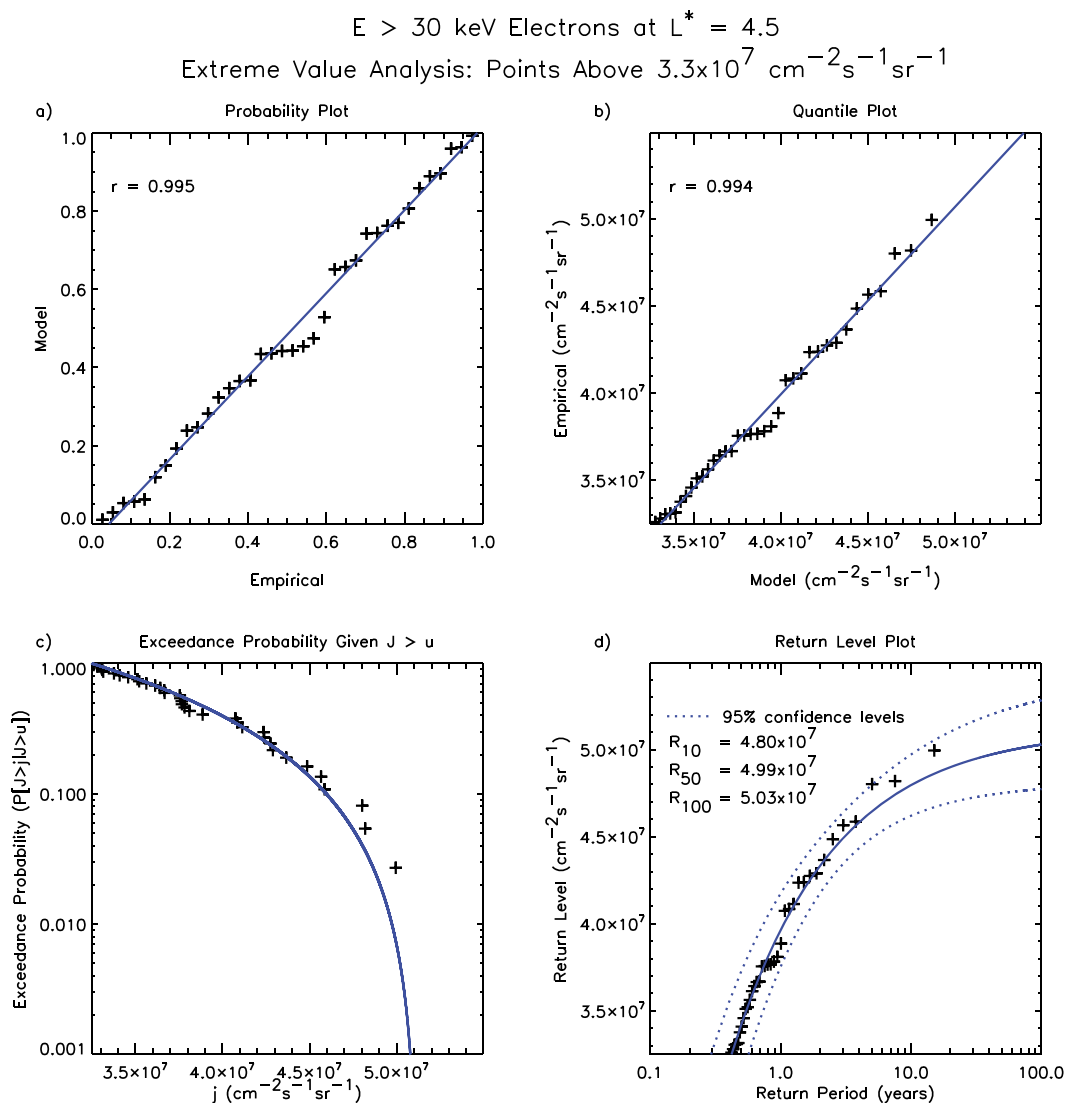


Figure 5. Extreme value analysis for the $E > 30$ keV electron flux at $L^* = 4.5$. (a) probability plot, (b) quantile plot, (c) the exceedance probability given $J > u$, and (d) the return level plot.

[*R Foundation for Statistical Computing*, 2008]. For each energy and L^* we set the threshold at the 0.1% exceedance level for the given energy and L^* . We then computed the 1 in N year events as a function of energy and L^* .

5. Results

To illustrate the extreme value analysis, we consider the flux of $E > 30$ keV electrons near the peak in their flux as a function of L^* at $L^* = 4.5$. This flux is shown in Figure 4 (top) as a function of UT, together with a trace of the sunspot number (bottom). The 0.1% exceedance level of $3.3 \times 10^7 \text{ cm}^{-2} \text{ s}^{-1} \text{ sr}^{-1}$, chosen as the threshold for the extreme value analysis, is marked as a dotted line. Cluster maxima are coded red. These are the values that are used in the extreme value analysis. The flux of $E > 30$ keV electrons exceeds the threshold around solar maximum and during the declining phase of the solar cycle being most frequent during the declining phase.

For the data collected at $L^* = 4.5$ the maximum likelihood estimates of the scale and shape parameters are $(1.0 \pm 0.005) \times 10^6$ and -0.55 ± 0.05 , respectively. Here the quoted error is the standard error. The shape parameter is negative suggesting that the distribution has an upper limit. The probability plot, showing the

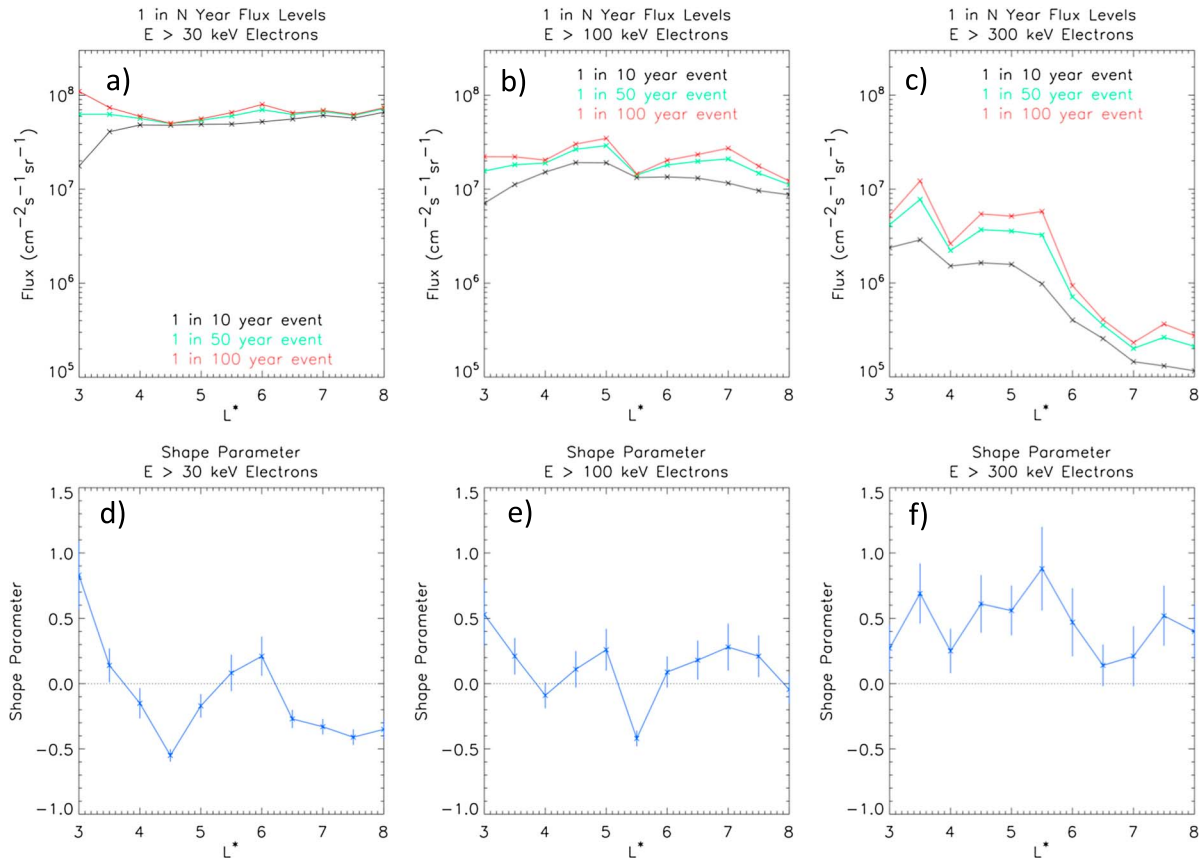


Figure 6. Plots of the 1 in N year flux level as a function of L^* for $N = 10$ (black), 50 (green), and 100 (red) for (a) $E > 30$ keV, (b) $E > 100$ keV, and (c) $E > 300$ keV electron fluxes and the shape parameter as a function of L^* for (d) $E > 30$ keV, (e) $E > 100$ keV, and (f) $E > 300$ keV electrons.

modeled and empirical probabilities, for the cluster maxima of $E > 30$ keV electrons is shown in Figure 5a. The blue line represents the best fit straight line to the data points using simple linear regression and has a correlation coefficient of 0.995. The corresponding quantile plot, showing the empirical and modeled quantiles, for the cluster maxima of $E > 30$ keV electrons is shown in Figure 5b. The blue line represents the best fit straight line to the data using simple linear regression and has a correlation coefficient of 0.994. Both fits are approximately linear illustrating that the generalized Pareto model is a good method for modeling the exceedances. The exceedance probability of the cluster maxima above the threshold value of $3.3 \times 10^7 \text{ cm}^{-2} \text{ s}^{-1} \text{ sr}^{-1}$ ($P[J > j | J > u]$) is shown in Figure 5c (black symbols), together with the maximum likelihood fit (blue line). The return level plot, showing the level that is exceeded on average once every N years as a function of N , for the declustered $E > 30$ keV electron flux is shown in Figure 5d. The symbols represent the experimental return levels, and the solid blue line represents the 1 in N year return level determined from equation (5). The dotted blue lines represent the 95% confidence interval of the 1 in N year return level. The 1 in 10, 1 in 50, and 1 in 100 year $E > 30$ keV electron fluxes at $L^* = 4.5$ are 4.8×10^7 , 5.0×10^7 , and $5.0 \times 10^7 \text{ cm}^{-2} \text{ s}^{-1} \text{ sr}^{-1}$, respectively. At this L^* the fluxes tend to a limit relatively quickly with differences between the 1 in 50 and 1 in 100 year event only being noticeable when the results are quoted to three significant figures (Figure 5d).

We repeated the extreme value analysis of the $E > 30$ keV electrons for other values of L^* and determined the corresponding 1 in N year events. The results are shown in Figure 6a for $N = 10, 50$, and 100 years. The 1 in 10 year flux (black line) shows a general increasing trend with distance ranging from $1.8 \times 10^7 \text{ cm}^{-2} \text{ s}^{-1} \text{ sr}^{-1}$ at $L^* = 3.0$ to $6.6 \times 10^7 \text{ cm}^{-2} \text{ s}^{-1} \text{ sr}^{-1}$ at $L^* = 8.0$. The 1 in 100 year flux (red line) lies in the range 5.0×10^7 to $1.1 \times 10^8 \text{ cm}^{-2} \text{ s}^{-1} \text{ sr}^{-1}$ and is generally a factor of 1.1 to 1.5 larger than the corresponding 1 in 10 year

event. The shape parameter for the $E > 30$ keV electrons is shown as a function of L^* in Figure 6d. In the region $3.5 \leq L^* \leq 8$ the shape parameter is predominantly negative, suggesting that the flux of $E > 30$ keV electrons has an upper bound. The limiting value, x_L , can be calculated for each L^* and is given by

$$x_L = u - \frac{\sigma}{\xi}. \quad (7)$$

The limiting value lies in the range 5.1×10^7 to $8.8 \times 10^7 \text{ cm}^{-2} \text{ s}^{-1} \text{ sr}^{-1}$.

We then performed an extreme value analysis of the flux of $E > 100$ keV electrons as a function of L^* . The resulting 1 in N year flux for $E > 100$ keV electrons is shown as a function of L^* in Figure 6b for $N = 10, 50$, and 100 years. The 1 in 10 year event (black line) peaks at $1.9 \times 10^7 \text{ cm}^{-2} \text{ s}^{-1} \text{ sr}^{-1}$ at $L^* = 4.5\text{--}5.0$ decreasing to minima of 7.1×10^6 and $8.7 \times 10^6 \text{ cm}^{-2} \text{ s}^{-1} \text{ sr}^{-1}$ at $L^* = 3.0$ and 8.0 , respectively. The 1 in 100 year event is a factor of 1.1 to 3.1 larger than the corresponding 1 in 10 year event. The 1 in 100 year event (red line) has a maximum of $3.5 \times 10^7 \text{ cm}^{-2} \text{ s}^{-1} \text{ sr}^{-1}$ at $L^* = 5.0$ decreasing to minima of 2.2×10^7 and $1.2 \times 10^7 \text{ cm}^{-2} \text{ s}^{-1} \text{ sr}^{-1}$ at $L^* = 3.0$ and 8.0 , respectively. The shape parameter for the $E > 100$ keV electrons is shown as a function of L^* in Figure 6e. The shape parameter is predominantly positive suggesting that the flux of $E > 100$ keV electrons does not have an upper limit.

Finally, we analyzed the flux of $E > 300$ keV electrons. The 1 in N year flux for $E > 300$ keV electrons is shown as a function of L^* in Figure 6c for $N = 10, 50$, and 100. In contrast to the $E > 30$ keV electrons, the 1 in 10 year flux of $E > 300$ keV electrons shows a general decreasing trend with distance ranging from $2.4 \times 10^6 \text{ cm}^{-2} \text{ s}^{-1} \text{ sr}^{-1}$ at $L^* = 3.0$ to $1.2 \times 10^5 \text{ cm}^{-2} \text{ s}^{-1} \text{ sr}^{-1}$ at $L^* = 8.0$. The 1 in 100 year event (red line) is a factor of 1.7 to 5.9 larger than the corresponding 1 in 10 year event. The 1 in 100 year event has a maximum of $1.2 \times 10^7 \text{ cm}^{-2} \text{ s}^{-1} \text{ sr}^{-1}$ at $L^* = 3.5$. The shape parameter for the $E > 300$ keV electrons, shown as a function of L^* in Figure 6f, is predominantly positive suggesting that the flux of $E > 300$ keV electrons does not have an upper limit.

6. Discussion

The 1% exceedance levels for $E > 30$ keV and $E > 100$ keV electrons peak at $L^* = 5.0$ (Figures 3d and 3e). In contrast, the 1% exceedance levels for $E > 300$ keV electrons (Figure 3f) peak at much lower L^* , at $L^* = 3.5$. This is indicative of different processes primarily affecting the lower and higher-energy electrons. Electrons with energies of the order tens to ~ 100 keV are injected into the inner magnetosphere during storms and substorms [Cayton *et al.*, 1989], with stronger events able to penetrate to lower L^* values. These electrons subsequently form the seed population for higher-energy electrons [e.g., Baker *et al.*, 1998; Obara *et al.*, 2000]. During geoeffective storms and geoeffective high-speed solar wind streams they are accelerated to higher energies by enhanced radial diffusion [Hudson *et al.*, 1999; Elkington, 2006] and by resonant wave particle interactions with whistler mode chorus [e.g., Horne *et al.*, 2005a, 2005b; Thorne *et al.*, 2013]. The latter tends to be enhanced outside the plasmopause, primarily on the dawnside during active conditions [Meredith *et al.*, 2012]. The largest fluxes of $E > 300$ keV electrons are seen at $L^* = 3$ consistent with the location of the strongest acceleration during the most extreme events, such as the Halloween storms of 2003, when the plasmopause was pushed inside $L^* = 3$ [Baker *et al.*, 2004].

The fact that potentially large fluxes of energetic electrons can penetrate as low as $L^* = 3$ is a concern for the new method of launching satellites with electric orbit raising [Horne and Pitchford, 2015]. The situation is most severe at higher energies. For example, at the 0.1% exceedance level, the flux of $E > 300$ keV electrons at $L^* = 3$ is almost an order of magnitude higher than that at geosynchronous orbit, suggesting that satellites undergoing electric orbit raising will experience considerably more damaging radiation at these energies than those at geosynchronous orbit.

In the region $4.0 \leq L^* \leq 8.0$ the shape parameter for $E > 30$ keV electrons is predominantly negative (Figure 6d) suggesting an upper bound which our results suggest lies in the range 5.1×10^7 to $8.8 \times 10^7 \text{ cm}^{-2} \text{ s}^{-1} \text{ sr}^{-1}$. At higher energies the shape parameter for the $E > 100$ keV and $E > 300$ keV electrons is predominantly positive suggesting that there is no upper limit to the higher-energy electron fluxes and is consistent with our findings for relativistic electrons at geosynchronous orbit [Meredith *et al.*, 2015]. In contrast, O'Brien *et al.* [2007] found evidence for finite upper limits to electron fluxes from approximately 450 keV to several MeV throughout the outer radiation belt, although not all of the flux limits met their validity criteria. The contrasting results demonstrate the difficulty of determining the presence or absence of an upper bound

from current data sets and suggest that a definitive answer may require longer data sets. In reality there is likely to be an upper limit, set by some physical process or processes, but this is not evident from the analysis presented here.

It is interesting to compare our results with the SCATHA “worst-case” environment used for the assessment of surface charging (www.spennis.oma.be). During this event, which occurred on 24 April 1979 near geosynchronous orbit close to the geomagnetic equator [Mullen *et al.*, 1981], the flux of electrons in the energy range $E > 30$ keV reached $7.4 \times 10^8 \text{ cm}^{-2} \text{ s}^{-1} \text{ sr}^{-1}$. This is about a factor of 14 larger than the 1 in 10 year event determined from the POES satellites in low Earth orbit on field lines that map out to geosynchronous orbit. The difference highlights the difficulty comparing observations in low Earth orbit with those in geosynchronous orbit as the former sample electrons with small equatorial pitch angles. For example, at POES altitudes an electron sampled by the T90 detector on a field line that maps to the magnetic equator at geosynchronous altitudes has an equatorial pitch angle of approximately 3° . In order to convert the low-altitude POES flux to a high-altitude equatorial flux, it is necessary to know the pitch angle distribution, which is not possible from low-altitude observations alone. This warrants further investigation, especially during large and extreme events, to see if it is possible to use the low-altitude measurements to estimate fluxes in the equatorial plane.

The second largest flux of $E > 300$ keV electrons at $L^* = 6.0$, on field lines that map out close to geosynchronous orbit, occurred on 5 April 2010 from 09 to 12 UT, encompassing the time Galaxy 15 ceased responding to commands from the ground. The maximum observed flux levels for the $E > 30$ keV, $E > 100$ keV, and $E > 300$ keV of $2.9 \times 10^7 \text{ cm}^{-2} \text{ s}^{-1} \text{ sr}^{-1}$, $9.8 \times 10^6 \text{ cm}^{-2} \text{ s}^{-1} \text{ sr}^{-1}$, and $4.3 \times 10^5 \text{ cm}^{-2} \text{ s}^{-1} \text{ sr}^{-1}$ correspond to 1 in 0.3, 1 in 2.2, and 1 in 9.6 year events respectively, suggesting that this event was more extreme at the higher energies. Interestingly, the fluxes of relativistic electrons were not elevated during this interval (Figure 2). These results suggest that the anomaly may have been caused by the unusually high levels of fluxes above ~ 100 keV but not at relativistic energies and are consistent with previous suggestions that the failure was due to enhanced fluxes of 200–600 keV electrons [Ferguson *et al.*, 2011; Loto'aniu *et al.*, 2015].

Two of the top five largest fluxes of $E > 300$ keV electrons at $L^* = 6.0$ occurred in late July 2004. These events occurred during the three strong storms that eventually lead to the largest flux of $E > 2$ MeV electrons observed at GOES over the 20 year period from 1995 to 2014 [Meredith *et al.*, 2015]. During this event Galaxy 10R lost its secondary ion propulsion system, used to maintain its in-orbit position, reducing its lifetime significantly [Choi *et al.*, 2011] and resulting in an insurance payout of U.S. \$75.3 million (Seradata SpaceTrak Launch and Satellite Database, www.seradata.com).

7. Conclusions

We have conducted an extreme value analysis of the maximum 3-hourly flux of $E > 30$, $E > 100$, and $E > 300$ keV flux as a function of L^* from the NOAA POES satellites for the 16 year period from 1 July 1998 to 30 June 2014. Our principle results are as follows:

1. The 1 in 10 year flux of $E > 30$ keV electrons shows a general increasing trend with distance ranging from $1.8 \times 10^7 \text{ cm}^{-2} \text{ s}^{-1} \text{ sr}^{-1}$ at $L^* = 3.0$ to $6.6 \times 10^7 \text{ cm}^{-2} \text{ s}^{-1} \text{ sr}^{-1}$ at $L^* = 8.0$.
2. The 1 in 100 year flux of $E > 30$ keV electrons lies in the range 5.0×10^7 to $1.1 \times 10^8 \text{ cm}^{-2} \text{ s}^{-1} \text{ sr}^{-1}$ and is generally a factor of 1.1 to 1.5 times larger than the corresponding 1 in 10 year event.
3. The 1 in 10 year flux of $E > 100$ keV electrons peaks at $1.9 \times 10^7 \text{ cm}^{-2} \text{ s}^{-1} \text{ sr}^{-1}$ at $L^* = 4.5$ – 5.0 decreasing to minima of 7.1×10^6 and $8.7 \times 10^6 \text{ cm}^{-2} \text{ s}^{-1} \text{ sr}^{-1}$ at $L^* = 3.0$ and 8.0 , respectively.
4. The 1 in 100 year flux of $E > 100$ keV electrons has a maximum of $3.5 \times 10^7 \text{ cm}^{-2} \text{ s}^{-1} \text{ sr}^{-1}$ at $L^* = 5.0$ decreasing to minima of 2.2×10^7 and $1.2 \times 10^7 \text{ cm}^{-2} \text{ s}^{-1} \text{ sr}^{-1}$ at $L^* = 3.0$ and 8.0 , respectively, and is a factor of 1.1 to 3.1 times larger than the corresponding 1 in 10 year event.
5. The 1 in 10 year flux of $E > 300$ keV electrons shows a general decreasing trend with distance ranging from $2.4 \times 10^6 \text{ cm}^{-2} \text{ s}^{-1} \text{ sr}^{-1}$ at $L^* = 3.0$ to $1.2 \times 10^5 \text{ cm}^{-2} \text{ s}^{-1} \text{ sr}^{-1}$ at $L^* = 8.0$.
6. The 1 in 100 year flux of $E > 300$ keV electrons is a factor of 1.7 to 5.9 larger than the corresponding 1 in 10 year event. The 1 in 100 year event has a maximum of $1.2 \times 10^7 \text{ cm}^{-2} \text{ s}^{-1} \text{ sr}^{-1}$ at $L^* = 3.5$.
7. The shape parameter is predominantly negative for the $E > 30$ keV electrons suggesting that the lower energy fluxes have an upper bound. Our results suggest that the limiting value lies in the range 5.1×10^7 to $8.8 \times 10^7 \text{ cm}^{-2} \text{ s}^{-1} \text{ sr}^{-1}$.
8. The shape parameter is predominantly positive for the $E > 100$ keV and $E > 300$ keV electrons suggesting that there is no upper bound for the fluxes of the higher-energy electrons. In reality there should be a

physical process that sets an upper limit, but this is not evident from the statistical analysis of the ~15 year data set presented here.

The 1 in N year flux levels as a function of energy and L^* computed here serve as benchmarks against which to compare other space weather events in low Earth orbit. The results may also be used to compute the return period of any given space weather event as a function of energy and L^* to determine if the event was particularly extreme at any given energy or location.

Acknowledgments

We would like to thank Justin Likar, David Pitchford, and David Wade for their useful discussions. We acknowledge the NOAA National Geophysical Data Center, now called the National Centers for Environmental Information, for the provision of the POES energetic particle data used in this study. The UNILIB library used in this study was developed by the Belgian Institute for Space Aeronomy under ESA/GSTP funding and is available at <http://www.mag-unilib.eu/>. The research leading to these results has received funding from the Natural Environment Research Council and the European Union Seventh Framework Programme (FP7/2007-2013) under grant agreement 606716 (SPACESTORM). The data used to generate the plots in this paper are stored at the BAS Polar Data Center and are available on request.

References

- Baker, D. N., X. Li, J. B. Blake, and S. G. Kanekal (1998), Strong electron acceleration in the Earth's magnetosphere, *Adv. Space Res.*, *21*(4), 609–613.
- Baker, D. N., S. G. Kanekal, X. Li, S. P. Monk, J. Goldstein, and J. L. Burch (2004), An extreme distortion of the Van Allen belt arising from the "Halloween" solar storm in 2003, *Nature*, *432*, 878–881, doi:10.1038/nature03116.
- Cabinet Office (2012), National Risk Register of Civil Emergencies. 70 Whitehall, London SW1A 2WH. [Available at www.cabinetoffice.gov.uk/.]
- Cayton, T. E., R. D. Belian, S. P. Gary, T. A. Fritz, and D. N. Baker (1989), Energetic electron components at geosynchronous orbit, *Geophys. Res. Lett.*, *16*(2), 147–150, doi:10.1029/GL016i002p00147.
- Choi, H.-S., J. Lee, K.-S. Cho, Y.-S. Kwak, I.-H. Cho, Y.-D. Park, Y.-H. Kim, D. N. Baker, G. D. Reeves, and D.-K. Lee (2011), Analysis of GEO spacecraft anomalies: Space weather relationships, *Space Weather*, *9*, S06001, doi:10.1029/2010SW000597.
- Coles, S. (2001), *An Introduction to Statistical Modelling of Extreme Values*, Springer, London.
- Della-Marta, P. M., H. Mathis, C. Frei, M. A. Liniger, J. Kleinn, and C. Appenzeller (2009), The return period of wind storms over Europe, *Int. J. Climatol.*, *29*, 437–459, doi:10.1002/joc.1794.
- Elkington, S. R. (2006), A review of ULF interactions with radiation belt electrons, in *Magnetospheric ULF Waves: Synthesis and New Directions*, vol. 169, edited by K. Takahashi et al., pp. 177–193, AGU, Washington, D. C.
- Evans, D. S., and M. S. Greer (2004), Polar Orbiting Environmental Satellite Space Environment Monitor-2: Instrument descriptions and archive data documentation, *NOAA Tech. Mem.* 93, version 1.4, Space Weather Predict. Cent., Boulder, Colo.
- Ferguson, D. C., W. Denig, and J. V. Rodriguez (2011), Plasma conditions during the Galaxy 15 anomaly and the possibility of ESD from subsurface charging. AIAA-2011-1061 presented at 49th AIAA Aerospace Sciences Meeting including the New Horizons Forum and Aerospace Exposition, Orlando, Fla., 15 Sept.
- Gubby, R., and J. Evans (2002), Space environment effects and satellite design, *J. Atmos. Sol. Terr. Phys.*, *64*, 1723–1733.
- Heffernan, J. E., A. G. Stephenson, and E. Gilleland (2014), ISMEV: An introduction to statistical modeling of extreme values. version 1.39. [Available at <http://www.ral.ucar.edu/ericg/softextreme.php>.]
- Horne, R. B., and D. Pitchford (2015), Space weather concerns for all-electric propulsion satellites, *Space Weather*, *13*, 430–433, doi:10.1002/2015SW001198.
- Horne, R. B., et al. (2005a), Wave acceleration of electrons in the Van Allen radiation belts, *Nature*, *437*, 227–230, doi:10.1038/nature03939.
- Horne, R. B., R. M. Thorne, S. A. Glauert, J. M. Albert, N. P. Meredith, and R. R. Anderson (2005b), Timescale for radiation belt electron acceleration by whistler mode chorus waves, *J. Geophys. Res.*, *110*, A03225, doi:10.1029/2004JA010811.
- Hudson, M. K., S. R. Elkington, J. G. Lyon, C. C. Goodrich, and T. J. Rosenberg (1999), Simulation of radiation belt dynamics driven by solar wind variations, in *Sun-Earth Plasma Connections*, vol. 109, edited by J. L. Burch, R. L. Carovillano, and S. K. Antiochos, pp. 171–182, AGU, Washington D. C.
- Koons, H. C. (2001), Statistical analysis of extreme values in space science, *J. Geophys. Res.*, *106*(A6), 10,915–10,921, doi:10.1029/2000JA000234.
- Koons, H. C., and D. J. Gorney (1992), The relationship between electrostatic discharges on spacecraft P78-2 and the electron environment, *J. Spacecr. Rockets*, *28*(6), 683–688, doi:10.2514/3.26300.
- Koons, H. C., and J. F. Fennell (2006), Space weather effects on communications satellites. The Radio Science Bulletin, International Union of Radio Science (URSI), 316, 27–41 March.
- Krausmann, E. (2011), The Space-Weather Awareness Dialogue: Findings and Outlook, *JRC Sci. and Tech. Rep.*, Publ. Off. of the Eur. Union, Brussels, Belgium.
- Lam, M. M., R. B. Horne, N. P. Meredith, S. A. Glauert, T. Moffat-Griffin, and J. C. Green (2010), Origin of energetic electron precipitation > 30 keV into the atmosphere, *J. Geophys. Res.*, *115*, A00F08, doi:10.1029/2009JA014619.
- Li, Y., W. Cai, and E. P. Campbell (2005), Statistical modeling of extreme rainfall in southwest Western Australia, *J. Clim.*, *18*, 852–863.
- Loto'aniu, T. M., H. J. Singer, J. V. Rodriguez, J. Green, W. Denig, D. Biesecker, and V. Angelopoulos (2015), Space weather conditions during the Galaxy 15 spacecraft anomaly, *Space Weather*, *13*, 484–502, doi:10.1002/2015SW001239.
- Maejima, H., S. Kawakita, H. Kusawake, M. Takahashi, T. Goka, T. Kurosaki, M. Nakamura, K. Toyoda, and M. Chu (2004), Investigation of power system failure of a LEO satellite. AIAA-2004-5657 presented at 2nd International Energy Conversion Engineering Conference, Providence, Rhode Island, 16–19 Aug.
- Meredith, N. P., R. B. Horne, A. Sicard-Piet, D. Boscher, K. H. Yearby, W. Li, and R. M. Thorne (2012), Global model of lower band and upper band chorus from multiple satellite observations, *J. Geophys. Res.*, *117*, A10225, doi:10.1029/2012JA017978.
- Meredith, N. P., R. B. Horne, J. D. Isles, and J. V. Rodriguez (2015), Extreme relativistic electron fluxes at geosynchronous orbit: Analysis of GOES E > 2MeV electrons, *Space Weather*, *13*, 170–184, doi:10.1002/2014SW001143.
- Mullen, E. G., M. S. Gussenhoven, and H. B. Garrett (1981), A "Worst Case" Spacecraft Charging Environment as Observed by SCATHA on 24 April 1979, *AFGL-TR-81-0231*, AFGL, Hanscom Air Force Base, Mass.
- Nogaj, M., P. Yiou, S. Parey, F. Malek, and P. Naveau (2006), Amplitude and frequency of temperature extremes over the North Atlantic region, *Geophys. Res. Lett.*, *33*, L10801, doi:10.1029/2005GL024251.
- Odenwald, S. F., and J. L. Green (2007), Forecasting the impact of an 1859-caliber superstorm on geosynchronous Earth-orbiting satellites: Transponder resources, *Space Weather*, *5*, S06002, doi:10.1029/2006SW000262.
- Obara, T., T. Nagatsuma, M. Den, Y. Miyoshi, and A. Morioka (2000), Main phase creation of "seed" electrons in the outer radiation belt, *Earth Planets Space*, *52*, 41–47.
- O'Brien, T. P., J. F. Fennell, J. L. Roeder, and G. D. Reeves (2007), Extreme electron fluxes in the outer zone, *Space Weather*, *5*, S01001, doi:10.1029/2006SW000240.

- Olson, W. P., and K. Pfizter (1977), Magnetospheric magnetic field modelling, *Annu. Sci. Rep.*, Air Force Off. of Sci. Res., Arlington, Va.
- Picklands, J. (1975), Statistical inference using extreme order statistics, *Ann. Stat.*, **3**, 119–131.
- R Development Core Team (2008), R: A language and environment for statistical computing. R Foundation for Statistical Computing, Vienna, Austria. [Available at <http://www.R-project.org>.]
- Rodger, C. J., M. A. Clilverd, J. C. Green, and M. M. Lam (2010a), Use of POES SEM-2 observations to examine radiation belt dynamics and energetic electron precipitation into the atmosphere, *J. Geophys. Res.*, **115**, A04202, doi:10.1029/2008JA014023.
- Rodger, C. J., B. R. Carson, S. A. Cummer, R. J. Gamble, M. A. Clilverd, J. C. Green, J.-A. Sauvaud, M. Parrot, and J.-J. Berthelier (2010b), Contrasting the efficiency of radiation belt losses caused by ducted and nonducted whistler-mode waves from ground-based transmitters, *J. Geophys. Res.*, **115**, A12208, doi:10.1029/2010JA015880.
- Rodgers, D. J., and K. A. Ryden (2001), Internal charging in space, spacecraft charging technology, in *Proceedings of the Seventh International Conference held 23-27 April, 2001 at ESTEC, ESA SP-476*, edited by R. A. Harris, pp. 25–32, Eur. Space Agency, Noordwijk, Netherlands.
- Roederer, J. G. (1970), *Dynamics of Geomagnetically Trapped Radiation*, Springer, 166 pp., New York.
- Satellite Industry Association (2015), State of the satellite industry report. [Available at www.sia.org/state-of-the-satellite-industry-report.]
- Strategic National Risk Assessment (2011), Department of Homeland Security, Washington, D. C. [Available at www.dhs.gov/strategic-national-risk-assessment-snra.]
- Tibaldi, C., B. H. Strauss, and C. E. Zervas (2012), Modelling sea level rise impacts on storm surges along US coasts, *Environ. Res. Lett.*, **7**, 014032, doi:10.1088/1748-9326/7/1/014032.
- Thomson, A. W. P., E. B. Dawson, and S. J. Reay (2011), Quantifying extreme behavior in geomagnetic activity, *Space Weather*, **9**, S10001, doi:10.1029/2011SW000696.
- Thorne, R. M., et al. (2013), Rapid local acceleration of relativistic radiation belt electrons by magnetospheric chorus, *Nature*, **504**, 411–414.
- Tsubouchi, K., and Y. Omura (2007), Long-term occurrence probabilities of intense geomagnetic storm events, *Space Weather*, **5**, S12003, doi:10.1029/2007SW000329.
- Viereck, R. (2012), The US-UK Space Weather Workshop, *Space Weather*, **10**, S04002, doi:10.1029/2012SW000770.
- Webb, D. F., and J. H. Allen (2004), Spacecraft and ground anomalies related to the October–November 2003 solar activity, *Space Weather*, **2**, S03008, doi:10.1029/2004SW000075.
- Wrenn, G. L. (1995), Conclusive evidence for internal dielectric charging anomalies on geosynchronous communications spacecraft, *J. Spacecr. Rockets*, **32**, 514–520.